processes

MDPI

Article

Experimental and CFD-Integrated Investigation into the Intricate Oil–Water Two-Phase Flow Dynamics Within Blind Tees: Uncovering Flow Behaviors for Advanced Process Engineering Applications

Chen Cheng [1,*], Qingming Gan [2], Yubin Su [2], Yang Cheng [3] and You Zhang [4,*]

[1] Sinopec Natural Gas Branch, Beijing 100020, China
[2] Oil & Gas Technology Research Institute, Changqing Oilfield Branch Company, PetroChina, Xi'an 710021, China; ganqm_cq@petrochina.com.cn (Q.G.); suyb_cq@petrochina.com.cn (Y.S.)
[3] Petroleum Engineering Technology Research Institute, Jianghan Oilfield Branch Company, Sinopec, Wuhan 430000, China; 18389599309@163.com
[4] Petroleum Engineering College, Yangtze University, Wuhan 430100, China
* Correspondence: chengchen_sinopec@163.com (C.C.); 15272424010@163.com (Y.Z.)

Abstract: Blind tees are widely used in offshore oil systems. To enhance their rectification performance, an indoor experimental platform was established to study the flow field behavior within blind tees and bend pipes. Fluent2021 analyzed the significant effects of various structural parameters and operating conditions on the oil–water rectification performance of blind tees. The study evaluates the device's effectiveness by establishing a rectification coefficient *S*, investigating the impacts of blind end length, vertical pipe diameter, inlet flow velocity, and inlet oil content. Results indicate that internal vortices within the blind tee primarily cause disturbances leading to uniform distribution of oil–water phases. The size and intensity of the vortices determine the oil–water rectification efficiency of the blind tee. Blind tees of different lengths correspond to a specific velocity at which the blind end becomes filled with vortices, causing fluid stagnation. This velocity is defined as the blind end closure velocity. Avoiding this closure velocity, shorter blind ends, smaller vertical pipe diameters, and higher inlet velocities significantly enhance the oil–water flow straightening effectiveness. The rectification efficiency of the blind tee was improved by up to76.68% compared to the bend.

Keywords: offshore oil pipelines; rectifiers; oil–water two-phase flow; CFD; vortex detection

check for updates

Academic Editors: Qingbang Meng and Tao Zhang

Received: 11 January 2025
Revised: 5 February 2025
Accepted: 19 February 2025
Published: 21 February 2025

Citation: Cheng, C.; Gan, Q.; Su, Y.; Cheng, Y.; Zhang, Y. Experimental and CFD-Integrated Investigation into the Intricate Oil–Water Two-Phase Flow Dynamics Within Blind Tees: Uncovering Flow Behaviors for Advanced Process Engineering Applications. *Processes* **2025**, *13*, 619. https://doi.org/10.3390/pr13030619

Copyright: © 2025 by the authors. Licensee MDPI, Basel, Switzerland. This article is an open access article distributed under the terms and conditions of the Creative Commons Attribution (CC BY) license (https://creativecommons.org/licenses/by/4.0/).

1. Introduction

Multiphase flow of oil and water is ubiquitous in the offshore oil industry, where crude oil often coexists with water, natural gas, and other components in many offshore oil fields [1]. Following gas–liquid separation, thorough research and precise measurement of oil–water two-phase flow are crucial for better understanding fluid behavior and flow characteristics. This understanding holds significant importance for assessing crude oil production, predicting the lifespan of oil well developments, monitoring well conditions, and enhancing energy efficiency [2]. However, the presence of significant phase slip within oil–water two-phase flow complicates measurements, necessitating the use of flow rectifiers before measurement instruments to improve accuracy [3]. Due to the scarcity of space on offshore drilling platforms, complex and massive rectifier devices are not suitable for installation, operation, and maintenance. The design and implementation of effective

and simple flow pattern rectifiers are, therefore, of paramount practical significance for multiphase flow measurements [4].

Bend configurations are the most common structural elements in subsea pipelines. Patankar et al. [5] successfully predicted the flow characteristics in curved pipes, encompassing both developing and fully developed flow regimes, by incorporating a two-equation turbulence model into a numerical solution method. Their predictions showed good agreement with experimental data, and the computational time remained within a reasonable range. The research of Hidesato et al. [6] demonstrated that varying hydrodynamic conditions at the inlet significantly influence flow behavior in bends; for instance, two serially connected 90° bends generate intense swirling flows downstream, depending on the combination angles. Liberto et al. [7] investigated turbulent flow in curved pipes with three curvature parameters (δ) using direct numerical simulation (DNS). Dutta [8] conducted a numerical study on turbulent single-phase flow in a circular 90° bend, focusing on the effects of different curvature ratios on flow characteristics. Noorani [9] investigated the influence of pipe curvature on the transport and accumulation of micro-particles. Ayala [10] performed a numerical study on turbulent flow in a smooth-walled circular 90° bend, aiming not only to estimate the resistance coefficient of the bend through pressure drop but also to incorporate information on downstream flow behavior in the outlet section. Additionally, Jarrahi [11] and Kim [12] systematically examined the swirling flow characteristics and mixing effects induced by 90° elbows.

The blind tee is a specialized pipe connection structure widely used in the petroleum and natural gas industries, distinguished from standard tees by having one closed end. Numerous scholars have conducted research on this structure. Pouraria found that blind tees exhibit greater erosion resistance for small diameter pipes; however, as pipe diameter increases, the erosion caused by blind tees can be comparable to or even more severe than that caused by standard bends [13]. Chen applied a CFD erosion prediction model to predict erosion in blind tees and bends under air/sand flow conditions, revealing significant influences of sand load on relative erosion severity. Tests under high sand concentrations showed that erosion in blind tees was two orders of magnitude less than that in bends [14]. Other studies have highlighted the blind tee's special promotion of heat and mass transfer within the fluid. Han used three-dimensional numerical simulations to study laminar flow within blind tees at Re = 500, 1000, 1500, and 2000, finding that higher flow velocities and blind tee lengths up to 3D facilitate good fluid mixing within the tee [15]. Ma installed blind tees upstream of Venturi meters and gamma-ray segments to measure oil, gas, and water three-phase flows, significantly improving measurement accuracy [16]. Bhakta observed that downstream of blind tee outlets, gas–liquid two-phase flows exhibit more symmetrical and uniform characteristics [17]. Millington described the variation in phase distribution at the outlet of the blind tee and the impact of inlet flow structures on mixing performance. Before the flow accelerated through a transparent plexiglass Venturi tube, phase area distribution was captured using an Electrical Capacitance Tomography (ECT) system in parallel with a high-speed video recorder. The results indicated that the mixing capability of the blind tee depends on the inlet flow patterns and oil viscosity, thereby affecting phase dispersion and slip characteristics through the Venturi section [18]. Experiments conducted by Hjertaker using a high-speed gamma-ray tomography instrument in the multiphase flow loop at the Christian Michelsen Research Institute demonstrated that near the blind tee, the flow is well mixed but significantly deviates from axisymmetry. Further up along the vertical pipe section, the flow develops towards an axisymmetric profile with increased slip. At lower flow rates, the vertical flow pattern develops more rapidly, resulting in a higher degree of axisymmetry, increased gas holdup in the pipe center, and greater slip between the gas and liquid phases [19]. In multiphase flow measurement systems, blind

tees are often used as flow mixers to homogenize the mixture when installed upstream of multiphase flow meters.

Based on a review of international research, it was found that studies on blind tees predominantly focus on erosion, single-phase flow, and the mixing characteristics of gas–liquid multiphase flow. However, there is limited research on the actual changes in the internal flow field of blind tees, their rectification effects on oil–water two-phase flow, and mixing mechanisms. Therefore, this study first investigated the actual changes in the internal flow field of blind tees through indoor experiments. Subsequently, different blind tee models with varying blind end lengths and vertical pipe diameters were established, and numerical simulations were used to explore the effects of different flow rates, blind end lengths, vertical pipe diameters, and inlet oil contents on the internal oil–water flow characteristics and rectification performance of blind tees. This research aims to provide references for the field of oil–water two-phase flow measurement and rectification.

2. Experimental Apparatus and Procedure

2.1. Experiment Set up and Measurement Techniques

To investigate the internal flow field patterns of blind tees and bend pipes, Particle Image Velocimetry (PIV) technology was used to conduct experiments on both structures. A flow pattern investigation experimental system was established at the Key Laboratory of Multiphase Flow in Yangtze University, which is shown in Figure 1. The system mainly consists of a liquid supply system, pipeline instrumentation, PIV measurement device (Hefei Zhongke Junda Vision Technology Co., Ltd., Hefei, China), and test sections. The experimental site is shown in Figure 2. In the experimental section, the bent pipe is a standard 90° bend with a diameter of 20 mm, while the blind tee has a main pipe diameter of 20 mm and a blind end length of 40 mm.

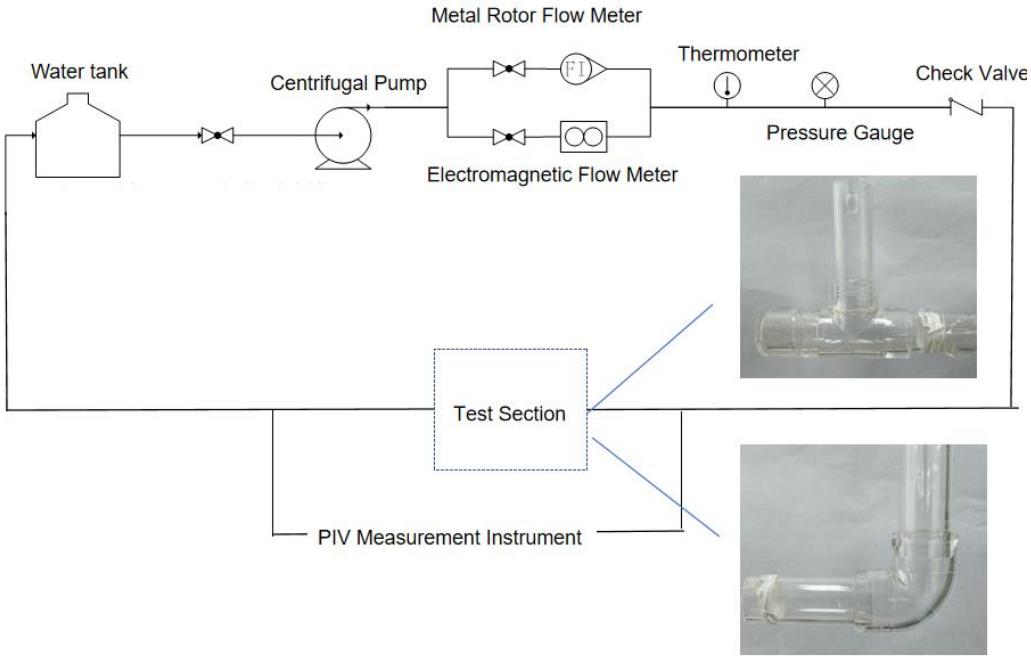


Figure 1. Schematic diagram and testing apparatus of experiment.

2.2. PIV Data Processing Techniques

The PIV data processing was performed using the manufacturer's proprietary software RFlow4 (Hefei Zhongke Junda Vision Technology Co., Ltd., Hefei, China), with a unique grid refinement function applied near the boundary wall to ensure that the closest measurement point to the boundary was half of the minimum diagnostic window size.

The calculation accuracy for both the velocity field and solid-phase particle motion was 0.1 pixels, with validation based on actual data from the PIV Challenge. Additionally, AI-based automatic masking, gamma correction, and high-pass filtering techniques were utilized in the data processing to reduce image noise.

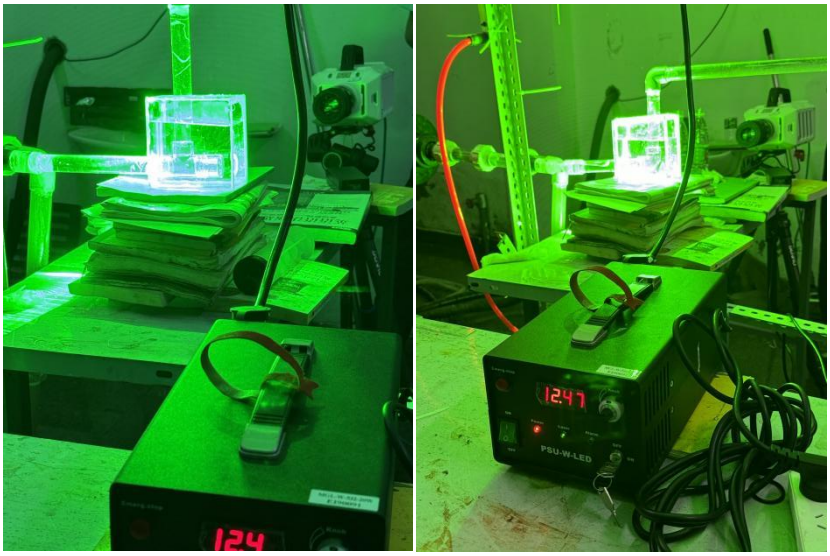


Figure 2. Experimental test site.

2.3. Experimental Conditions and Control

Since this experiment primarily focuses on the hydrodynamic behavior and vortex evolution mechanisms within blind tee and elbow structures, pure water was used as the working fluid to reduce experimental costs and enhance visualization of the internal flow characteristics. At 25 °C, the density of water is 998 kg/m^3, and the dynamic viscosity is 0.89 mPa·s. The volumetric flow rate was controlled by a variable-frequency pump set at 0.4 m^3/h. The experiment was conducted at 25 °C, with both inlet and outlet pressures maintained at atmospheric pressure to ensure consistency in boundary conditions.

The experimental apparatus was designed with a geometric scale ratio of 1:25 (model pipe diameter D = 20 mm, corresponding to a typical offshore pipeline prototype diameter of D_0 = 500 mm). The Reynolds number of the model was Re = 6995.88, and the calculated prototype Reynolds number was Re_0 = 70,382 (Q =100 m^3/h), both within the turbulent regime (Re > 4000), ensuring flow similarity.

To ensure the measurement accuracy of the PIV system, rigorous calibration and validation were performed prior to the experiment, including laser source adjustment, camera focal correction, and optimization of particle imaging quality. Additionally, three repeated measurements were conducted to evaluate data stability and minimize the influence of random errors. These experimental conditions ensured the stability of the working fluid, the consistency between the experimental environment and practical engineering conditions, and provided reliable visualization data for investigating the internal flow field evolution and vortex structures within blind tees and elbows.

2.4. Analysis of Experimental Results

In the design of flow rectifiers, the types and characteristics of vortices generated within the device serve as key indicators of rectification effectiveness [20–22]. Therefore, this study employed Particle Image Velocimetry (PIV) technology to detect vortices within the internal flow field. Figures 3 and 4, obtained using PIV post-processing software RFlow4, present the vector field and streamline plot of the blind end region of the blind tee, providing detailed insights into the flow characteristics and vortex generation mechanisms

of fluid within the blind end. The vector field arrows indicate that the rotational motion of the fluid within the blind end leads to the formation of lateral vortices, where the vortex core region exhibits lower velocity, while the outer region has higher velocity. The formation of these vortices is primarily due to the impact of the incoming fluid on the structural walls of the blind end, inducing localized rotational motion. This process facilitates the transfer of kinetic energy from the main flow into the vortex, establishing a primary energy dissipation region. The streamline plot further reveals the fluid motion paths and flow states within the blind end. Fluid particles within this region follow rotational streamlines, forming sustained recirculation and circular motion, significantly increasing fluid residence time in the blind end. This enhances energy exchange between fluid particles, thereby improving the rectification performance of the blind tee. Observing the vector arrows, it is evident that the vortex core region exhibits lower velocity, whereas velocity gradually increases at the interface between the vortex periphery and the main flow, forming a velocity gradient. This velocity distribution suggests that vortex formation is a primary contributor to kinetic energy dissipation, and that velocity gradients facilitate localized momentum balance and rectification effects. In the high-velocity regions near the blind end, fluid transfers energy from the main flow into the blind end, maintaining vortex stability. These analyses collectively highlight that the blind end structure plays a crucial role in regulating flow behavior, enhancing rectification performance, and promoting fluid mixing.

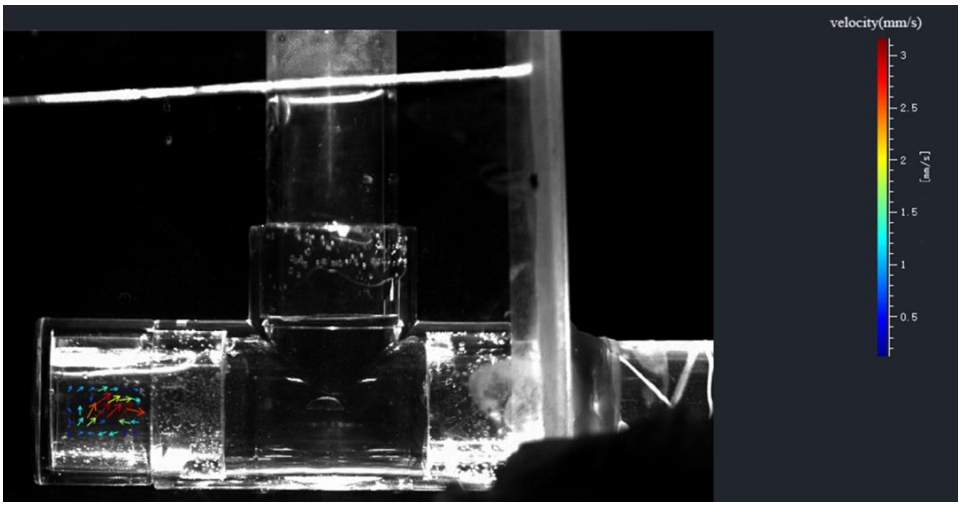


Figure 3. Flow vector diagram at the blind end of the blind tee.

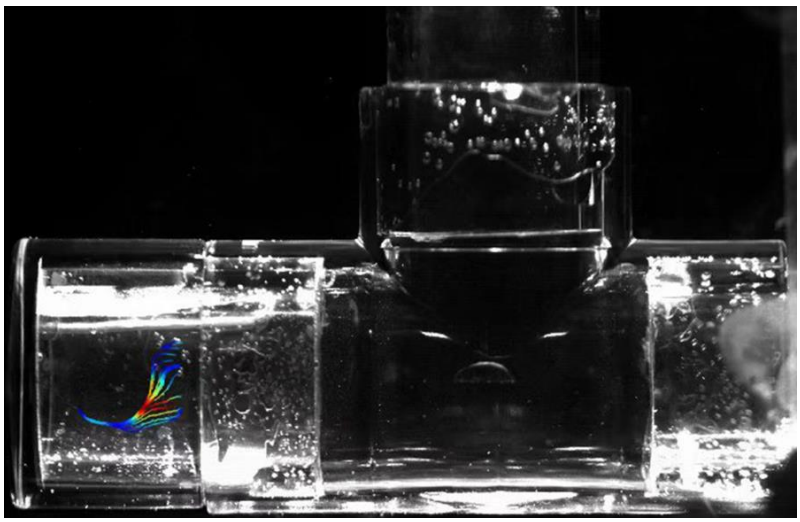


Figure 4. Streamline diagram at the blind end of the blind tee.

Figures 5 and 6 present the streamline plots of the turning regions in the blind tee and elbow. The streamline plots reveal that fluid flow in the turning regions of both the blind tee and elbow is influenced by centrifugal forces and geometric constraints, leading to the formation of a typical secondary flow structure. Fluid particles near the inner wall of the elbow exhibit recirculation, generating vortices in this region. The streamline distribution in the blind tee appears more disordered, indicating stronger mixing effects in two-phase flow. In contrast, the vortices in the elbow are smaller, but they still play a positive role in promoting fluid mixing. These findings demonstrate that the blind tee and elbow each exhibit unique flow dynamics in the turning regions, yet both induce vortex formation, which is critical in enhancing fluid mixing and rectification performance.

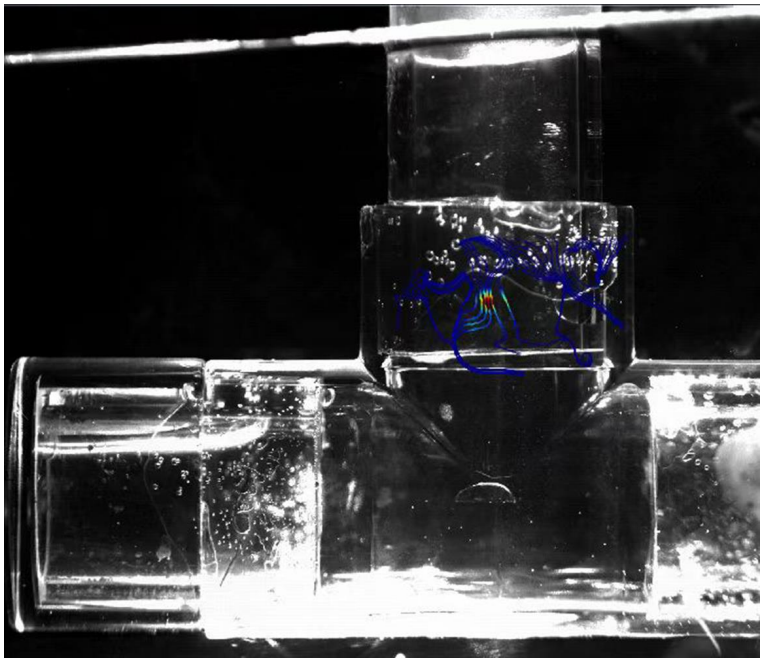


Figure 5. Streamline diagram at the elbow of the blind tee.

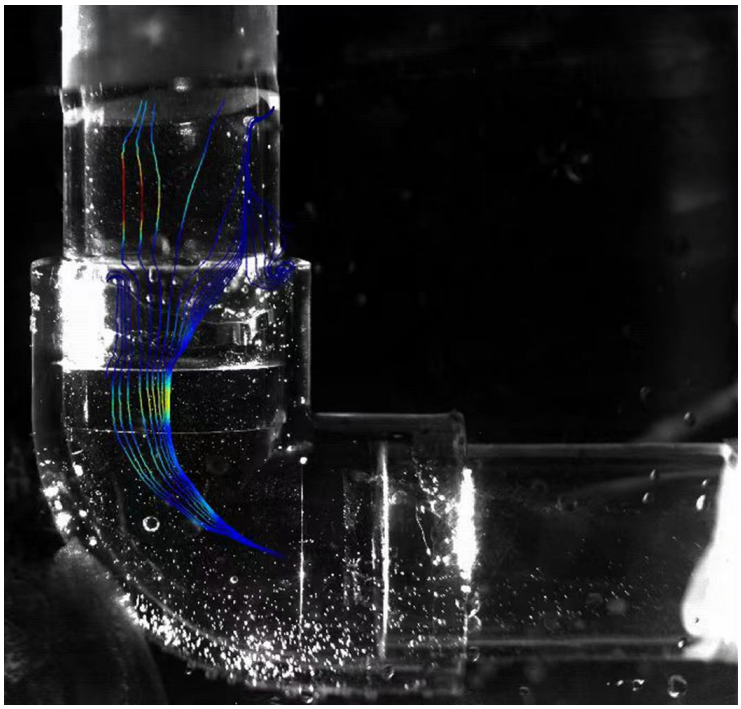


Figure 6. Streamline diagram at the elbow of the bend pipe.

This experiment provided deeper insights into the internal flow characteristics of the blind tee and elbow, which can also serve as a validation basis for subsequent numerical simulation studies.

3. Numerical Simulation

3.1. Geometric Model

A model of a blind tee with a blind end length of 1D and a vertical inner diameter of 40 mm is shown in Figure 7, where D is 40 mm, C is 20 mm, and L is 190 mm. In the subsequent simulations, D was set to 20 mm, 25 mm, 30 mm, 35 mm, and 40 mm; L was set to 190 mm, 210 mm, 230 mm, 250 mm, and 270 mm; and C was set to 20 mm, 40 mm, 60 mm, 80 mm, and 100 mm. To analyze the rectification effect on the oil–water two-phase flow, it was essential to ensure that the oil and water phases were in a non-homogeneous mixed state upon entering the device. Therefore, two inlets were configured: a pure water inlet for the water phase and an oil–water mixture inlet for the oil phase.

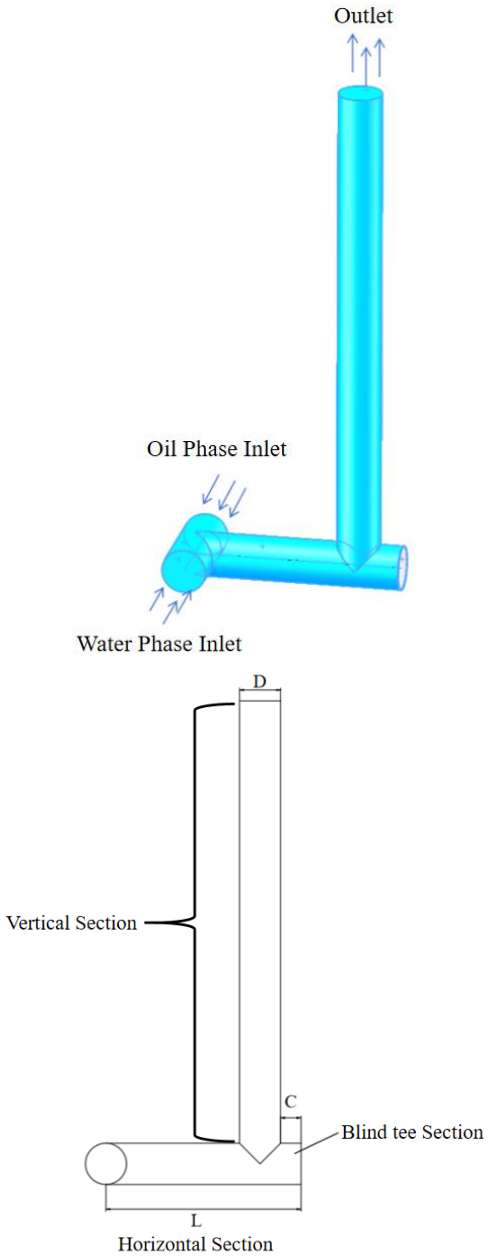


Figure 7. Blind tee mode.

3.2. Methodology

3.2.1. Multiphase Flow Model and Boundary Conditions

The multiphase flow model adopts the Eulerian model.

Continuity equation:

$$\frac{\partial}{\partial t}(\alpha_q \rho_q) + \nabla \cdot (\alpha_q \rho_q v_q) = \sum_p \dot{m}_{pq} \tag{1}$$

where α_q is the volume fraction of phase q, ρ_q is the density of phase q, v_q is the velocity of phase q, $\dot{m}_{pq}$ is the mass source term transferred from phase p to phase q, representing interphase mass exchange.

The momentum equation is expressed as follows:

$$\frac{\partial}{\partial t}(\alpha_q \rho_q v_q) + \nabla \cdot (\alpha_q \rho_q v_q v_q) = -\alpha_q \nabla P + \nabla \cdot (\tau_q) + \alpha_q \rho_q g + \sum_p M_{pq} \tag{2}$$

where P is the pressure, τ_q is the stress tensor of the phase q, g is the gravitational acceleration, M_{pq} is the interphase momentum exchange term.

The RNG (Renormalization Group) k-ε turbulence model was chosen for this simulation, as it accounted for the effects of swirl on turbulence viscosity, making it more effective in handling highly swirling and curved flows. A three-dimensional steady-state model was employed, and the SIMPLE (Semi-Implicit Method for Pressure-Linked Equations) algorithm was used for iterative calculations. In the numerical simulation, the turbulence intensity was set to 5%, which is a commonly used initial turbulence intensity value for industrial pipeline flows. A first-order discretization scheme was adopted, offering high computational efficiency and fast convergence, typically used for initial solutions or when high stability is required. The boundary layer thickness was set to 1.9 mm.

For the boundary conditions, the water phase inlet consisted of pure water, while the oil phase inlet consisted of oil–water mixtures with oil concentrations of 10%, 20%, 30%, 40%, and 50%. The inlet velocities were set at 1 m/s, 2 m/s, 3 m/s, 4 m/s, and 5 m/s, respectively.

3.2.2. Turbulence Model

In the RNG k-epsilon model, the influence of small-scale motions is accounted for through modified viscosity terms in the large-scale motion equations, systematically eliminating these small-scale effects from the governing equations [23]. The equations are as follows:

$$\frac{\partial(\rho K)}{\partial t} + \frac{\partial(\rho \overline{u_j} K)}{\partial x_j} = \frac{\partial}{\partial x_j}\left[\left(\mu + \frac{\mu_t}{Pr_K}\right)\frac{\partial K}{\partial x_j}\right] + P_K + G_b - \rho\varepsilon - Y_M \tag{3}$$

$$\frac{\partial(\rho \varepsilon)}{\partial t} + \frac{\partial(\rho \overline{u_j} \varepsilon)}{\partial x_j} = \frac{\partial}{\partial x_j}\left[\alpha_\varepsilon\left(\mu + \frac{\mu_t}{\mathrm{Pr}_\varepsilon}\right)\frac{\partial \varepsilon}{\partial x_j}\right] + C_{\varepsilon 1}\frac{\varepsilon}{K}(P_K + C_{\varepsilon 3} G_b) - C^*_{\varepsilon 2}\rho\frac{\varepsilon^2}{K} \tag{4}$$

In these equations:

$$\mu_t = C_\mu \rho \frac{K^2}{\varepsilon} \tag{5}$$

$$C^*_{\varepsilon^2} = C_{\varepsilon 2} + \frac{C_\mu \rho \eta^3 \left(1 - \frac{\eta}{\eta 0}\right)}{1 + \beta \eta^3} \tag{6}$$

$$\eta = \frac{K}{\varepsilon}\overline{S} \tag{7}$$

$$\overline{S} = \sqrt{2\overline{S}_{ij}\overline{S}_{ij}} \tag{8}$$

$$\overline{S}_{ij} = \frac{1}{2}\left(\frac{\partial \overline{u}_i}{\partial x_j} + \frac{\partial \overline{u}_j}{\partial x_i}\right) \tag{9}$$

where ρ is the fluid density, K is the turbulence kinetic energy, t is time, $\overline{u_j}$ is the mean velocity component in the j-th direction, x_j is the spatial coordinate in the j-direction, μ is dynamic viscosity, μ_t is turbulent viscosity, Pr_K is the Prandtl number for turbulence kinetic energy, P_K is the generation rate of turbulence kinetic energy, G_b is the turbulence kinetic energy generated by buoyancy, ε is the dissipation rate of turbulence kinetic energy, and Y_M is the influence of fluctuating dilation on the turbulence dissipation rate.

3.2.3. Grid Resolution Testing

The model was meshed using Fluent meshing, with refined meshes applied to the corner regions and 10 layers of boundary layers set, as shown in Figure 8. To validate the mesh accuracy, five different mesh models were established: mesh1 with 278,256 elements, mesh2 with 327,506 elements, mesh3 with 453,919 elements, mesh4 with 571,184 elements, and mesh5 with 678,590 elements for simulation. Figure 9 shows the velocity distribution along the x-axis at the outlet for each mesh model. It can be observed that the simulation results of the five models differ only slightly, with only one sampling point having an error of around 10%, while the errors at other sampling points remain within single digits. The reason is that the model is relatively simple, with no small regions requiring fine meshes for high-precision calculations. To ensure simulation accuracy and reduce simulation time, the mesh3 model with 453,919 elements was selected for the simulation study.

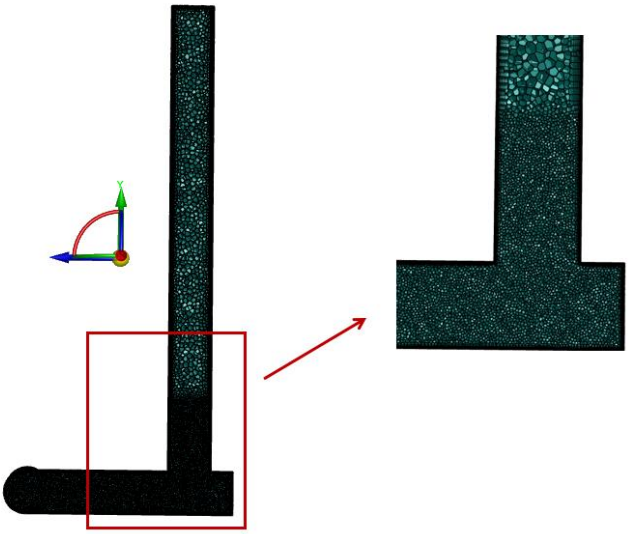


Figure 8. Mesh partitioning.

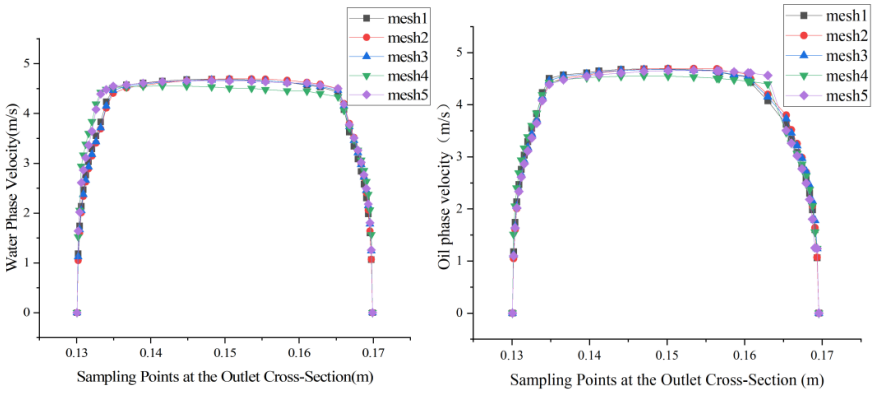


Figure 9. The velocity distributions of the water phase (**left**) and the oil phase (**right**) at the outlet under different mesh models.

3.3. Evaluation Mathematical Model

To quickly assess the rectification efficiency of the model, coefficient S was defined as the rectification coefficient, where its magnitude reflected the uniformity of flow patterns within the pipeline. An S value of 0 indicated perfect mixing, while increasing S values greater than 0 indicated increasing flow non-uniformity. The expression was given as follows:

$$S = \sqrt{\frac{1}{N}\sum_{i=1}^{N}\left(\rho_{x_i y_j} - \overline{\rho}\right)^2} \tag{10}$$

where N is the number of sampling points. A larger N indicates a more comprehensive evaluation of the rectification efficiency of the device by the mathematical model. $\rho_{x_i y_j}$ is the density of sampling points at different locations (in this study, points at the cross section y = 400 mm are selected to evaluate the rectification efficiency of the device) and $\overline{\rho}$ is the average density of the fluid entering the device.

3.4. Analysis of Simulation Results

3.4.1. Flow Characteristics of Oil–Water Two-Phase Flow Inside a Bent Pipe

To verify the superiority of the blind tee over traditional bent pipes in adjusting multiphase flow patterns, an internal flow field analysis was first conducted on a commonly used bent pipe in the petroleum industry. Numerical simulations were performed on a 90-degree bent pipe with a curvature radius of 1.5D, a diameter of 40 mm, a vertical length of 420 mm, and a horizontal length of 190 mm, followed by a detailed analysis of the internal flow field.

Figure 10 shows the schematic diagram of the bent pipe. Pure water was introduced at the water phase inlet, while an oil–water mixture with 40% oil content was introduced at the oil phase inlet. Figure 11 presents the phase distribution contour plot at the y = 0.002 m cross section. It can be observed that the fluids from both inlets collide in the middle of the pipe and flow into the bent section. In the bent section, the oil phase exhibits a trapezoidal distribution on the zx plane, indicating a highly turbulent state of oil–water two-phase flow. The inlet design of the model meets the requirement for non-uniform mixing of the two phases upon entry into the pipe.

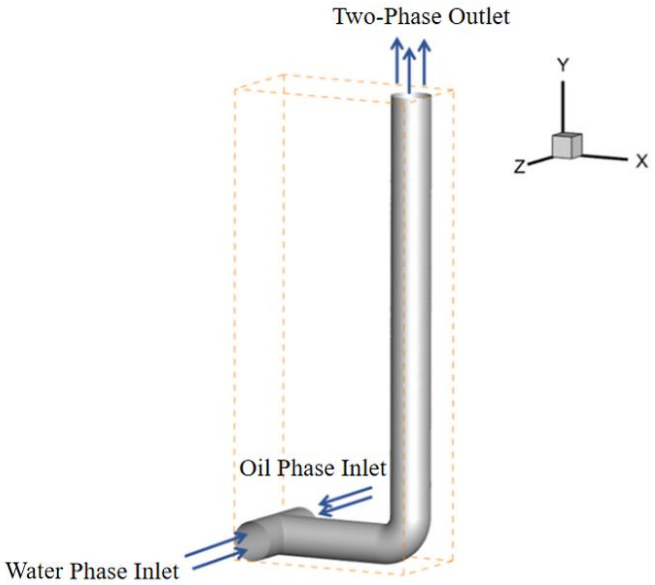


Figure 10. Schematic of bent pipe structure.

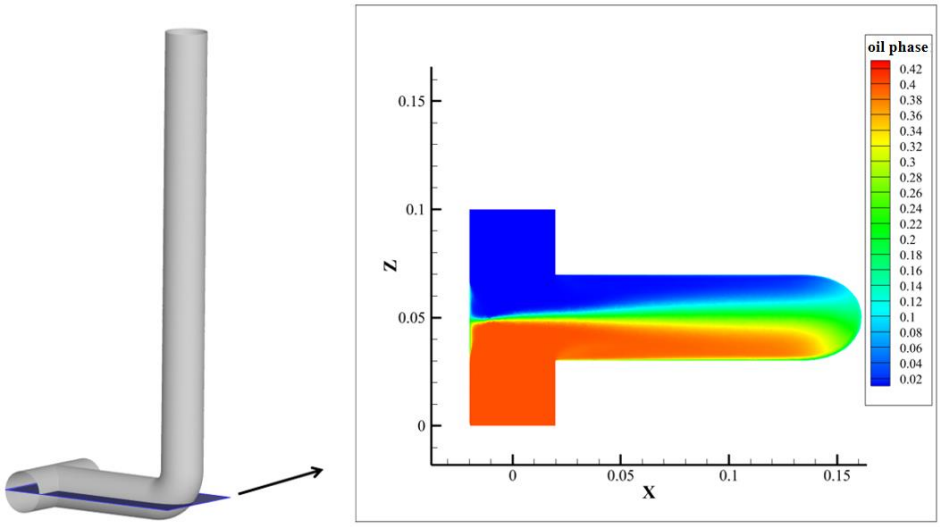


Figure 11. Phase distribution contour plot at cross section y = 0.002 m of bent pipe.

Figure 12 depicts the velocity and phase distribution contour plots of the oil–water two-phase flow at the z = 0.05 m cross section. The fluids from both inlets collide in the middle of the pipe, causing velocity superposition, which increases the fluid velocity in the horizontal pipe section from 1–2 m/s to approximately 5 m/s. As the oil–water flow enters the bend area, the fluid velocity near the inner side of the bend remains around 5 m/s, whereas the velocity near the outer side is noticeably lower. After exiting the bend, the high-speed fluid near the inner side flows towards the outer side of the vertical pipe section, where the fluid velocity is lower near the inner wall, forming a low-speed elliptical region. Comparison of the velocity and phase distribution contour plots at the z = 0.05 m cross section reveals significant overlap between the high-velocity region and the region with a high oil phase volume fraction near the bend. This indicates that the oil phase velocity exceeds the water phase velocity, suggesting significant velocity slip between the oil and water phases. These phenomena arise because the kinetic energy generated by the collision of inlet fluids results in velocity superposition. Due to the lower density of oil compared to water, the oil accelerates more rapidly. As the oil moves through the horizontal pipe section, buoyancy causes it to rise towards the inner side of the bend, resulting in higher fluid velocities near the inner side.

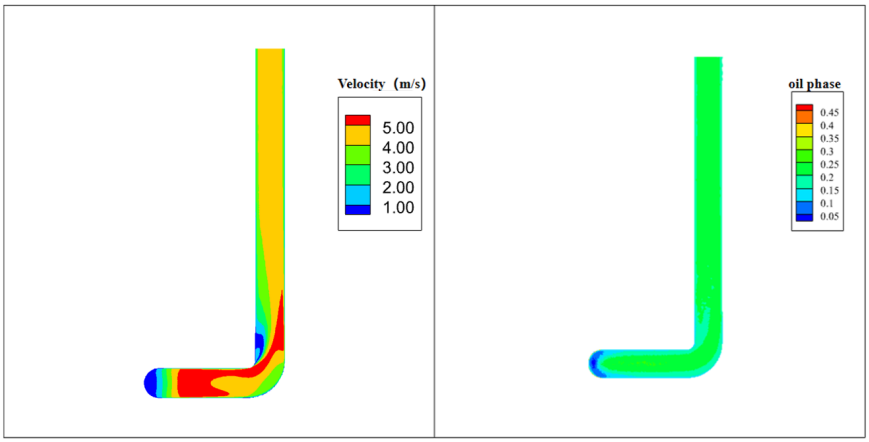


Figure 12. Velocity distribution contour plot (left) and phase distribution plot (right) of oil–water two-phase flow at cross section z = 0.05 m in the bent pipe.

Figures 13 and 14 present the velocity and phase distribution contour maps at different y-positions at the outlet of the bent pipe. After passing through the bend, the oil–water

velocity gradually increases from the inner side to the outer side, forming a trapezoidal distribution, where high-speed fluid accumulates near the outer wall, while low-speed fluid is concentrated near the inner wall. This velocity gradient enhances shear interaction between the fluids, promoting interphase momentum exchange and improving mixing efficiency. However, excessive velocity differences may lead to flow instability and even phase stratification, which, in severe cases, can reduce mixing uniformity. At the initial entrance into the curved section, the phase distribution trend is similar to that in the horizontal pipe, with oil content gradually decreasing along the *z*-axis. The presence of vortex structures affects the phase distribution, which, in turn, determines the configuration of the oil–water interface. When the phase distribution is uniform, vortices can disrupt the two-phase interface, allowing the oil phase to disperse more easily into the water phase, thereby improving mixing efficiency. However, if the phase distribution is uneven, the oil phase may accumulate in specific regions, leading to localized oil–water separation, which reduces both rectification and mixing performance. As the fluid flows downstream, the low-speed region on the inner side gradually shrinks. Due to the mixing of the water and oil phases, the velocity distribution becomes more uniform. The superposition of high-speed water flow and low-speed oil flow contributes to this uniformization phenomenon.

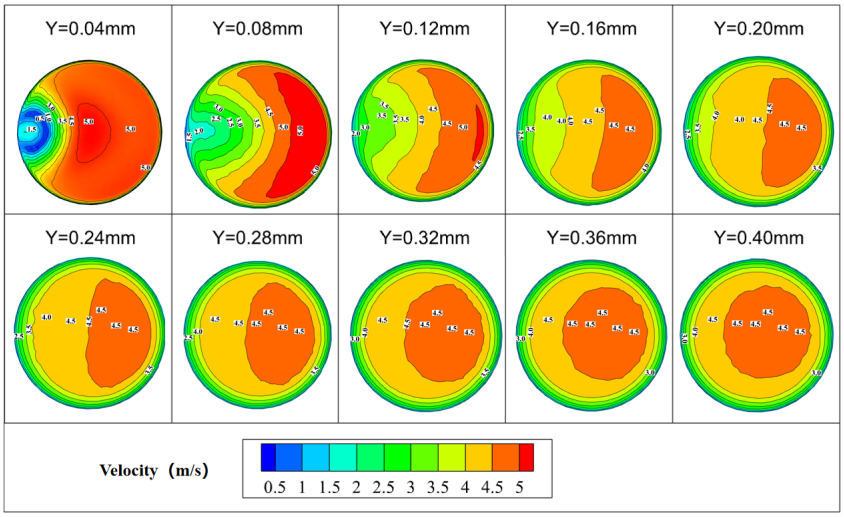


Figure 13. Velocity contour plots at cross sections of the outlet sections at different positions in the y-direction of the bent pipe.

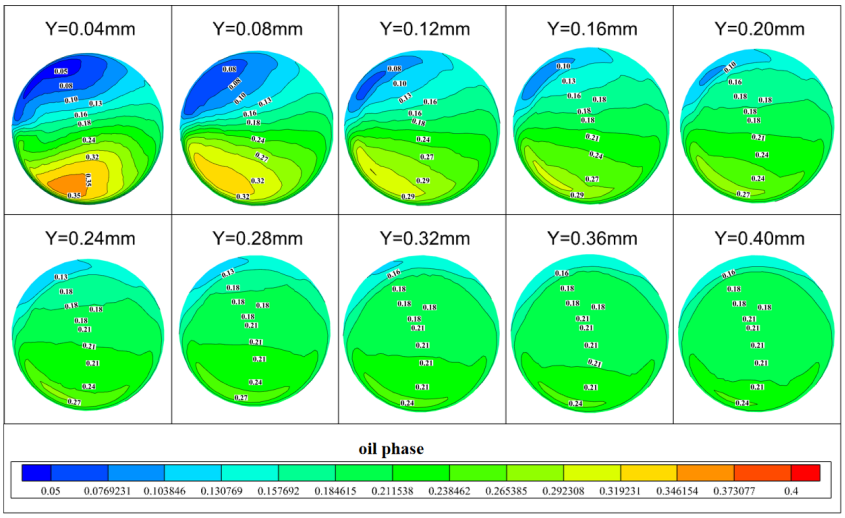


Figure 14. Phase distribution contour plots at cross sections of the outlet sections at different positions in the y-direction of the bent pipe.

Figure 15 shows that a longitudinal vortex generated at the bend causes streamlines from the outer side of the horizontal pipe to reach the inner side, forming secondary flow. This vortex disturbs the inner boundary layer, enhancing energy transfer and mixing efficiency, thereby further uniformizing the velocity and phase distribution. However, due to the limited number and intensity of vortices, the fluid requires a significant distance to achieve complete uniformity. The rectification coefficient of the bent pipe is 4.243, indicating suboptimal rectification performance.

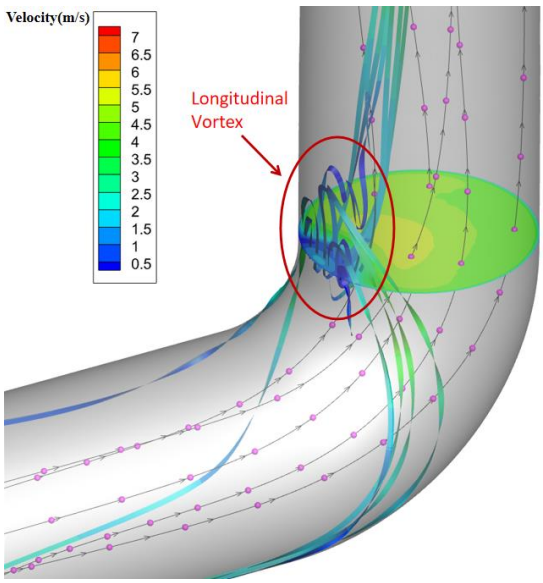


Figure 15. 3D streamline plot of the bent pipe.

3.4.2. Flow Characteristics of Oil–Water Two-Phase Flow Inside the Blind Tee

Taking a blind tee with a blind end of 1D as an example, the flow characteristics of oil–water two-phase flow inside were investigated. The inlet velocity was set to 2 m/s with an oil content of 0.2, and other conditions were kept consistent with the bent pipe. Figure 16 shows the velocity and phase distribution contour plots of the oil–water two-phase flow at the z = 0.05 m cross section. At the pipe bend, the flow velocity is similar to that in the bent pipe, with the high-velocity region extending along the upper wall of the bend to the outer wall of the vertical pipe. In this region, the oil phase volume fraction is also higher than in other areas. The velocity at the blind end is slightly lower than in the straight pipe section, with low-velocity regions appearing at the upper right and lower right corners. This is because the high-velocity fluid impacts the blind end, causing a change in direction and a significant decrease in velocity.

Figures 17 and 18 present velocity and phase distribution contours at the outlet cross sections of the blind tee at various y-positions. Post-bend, a low-velocity vortex forms along the left wall, extending to the pipe's center. As the flow progresses, the low-velocity fluid mixes with high-velocity fluid near the right wall, leading to a more uniform cross-sectional velocity distribution. The blind tee induces a more chaotic velocity distribution in the lower vertical section, but as the flow ascends, the velocity distributions of both the blind tee and bent pipe converge, indicating more effective velocity integration in the blind tee. Phase distribution patterns are consistent between the blind tee and bent pipe, though the blind tee exhibits smaller regions of maximum and minimum values at the y = 0.32 m cross section. By y = 0.4 m, the blind tee's low-velocity region diminishes, while the bent pipe still displays a significant low-velocity zone. The blind tee's rectification coefficient is 2.765, lower than the bent pipe's 4.243, confirming its superior rectification performance. The longitudinal vortex is a rotational flow structure extending along the main flow direc-

tion, primarily generated by wall shear effects, fluid inertia, and secondary flow induced by geometric perturbations. In the blind tee, the corner-induced longitudinal vortex enhances momentum exchange between the central region and near-wall areas, reducing velocity gradients between different flow layers, effectively preventing the formation of low-speed stagnant zones and thereby improving overall flow uniformity. Additionally, the rotational motion of the vortex induces fluid particles to rotate along the main flow direction, increasing turbulent kinetic energy and enhancing flow disturbances, which further improves internal fluid mixing uniformity. In contrast, the lateral vortex at the blind end is a rotational structure perpendicular to the main flow direction, generated by fluid impact on the structural wall. This vortex induces rolling motion in the fluid, enhancing molecular mixing, promoting interactions between different flow layers, and reducing concentration gradients, ultimately resulting in a more uniform phase distribution. As shown in Figure 19, the combined effect of the longitudinal and lateral vortices enables the blind tee to achieve superior mixing efficiency and rectification performance. Figure 20 compares the internal flow fields of both structures; despite the smaller longitudinal vortex in the blind tee, it extends to the pipe's center, affecting a larger fluid area. The blind end also generates significant vortices, enhancing internal mixing. Numerical simulations align with experimental results, underscoring the simulations' high reference value.

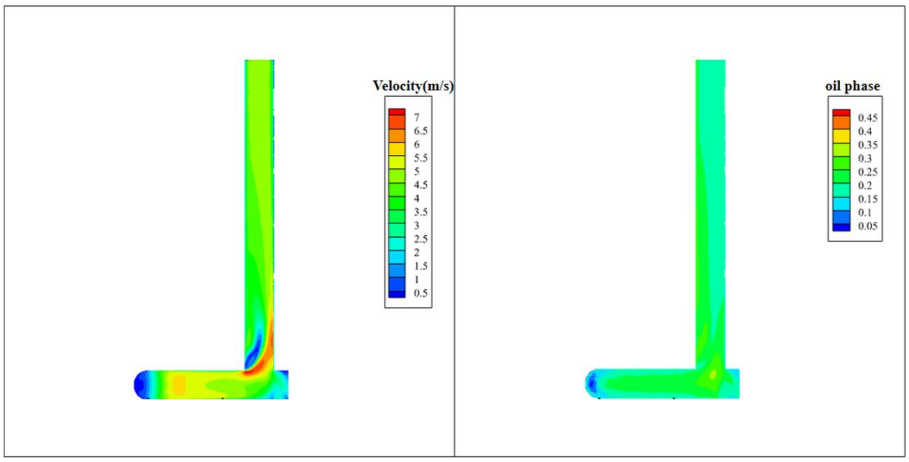


Figure 16. Velocity distribution contour plot (**left**) and phase distribution plot (**right**) of oil–water two-phase flow at cross section z = 0.05 m in the blind tee.

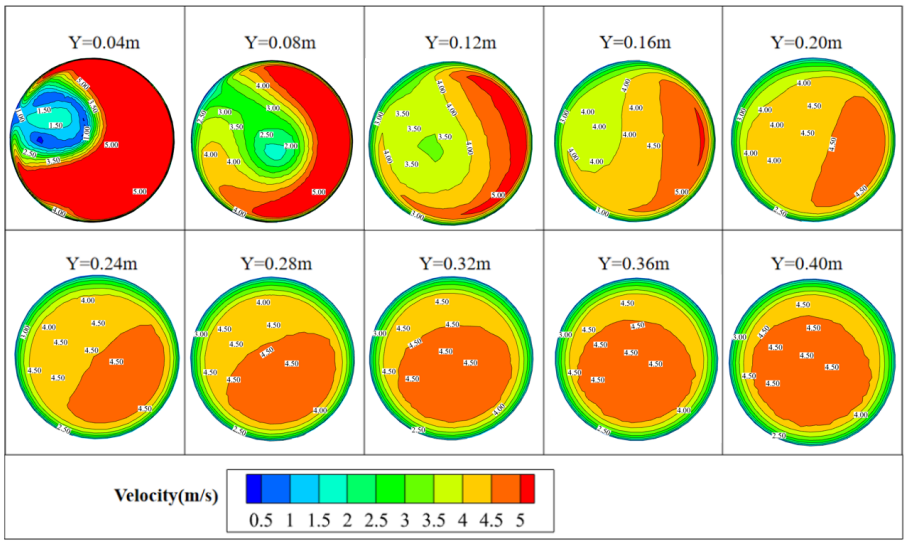


Figure 17. Velocity contour plots at cross sections of the outlet sections at different positions in the y-direction of the blind tee.

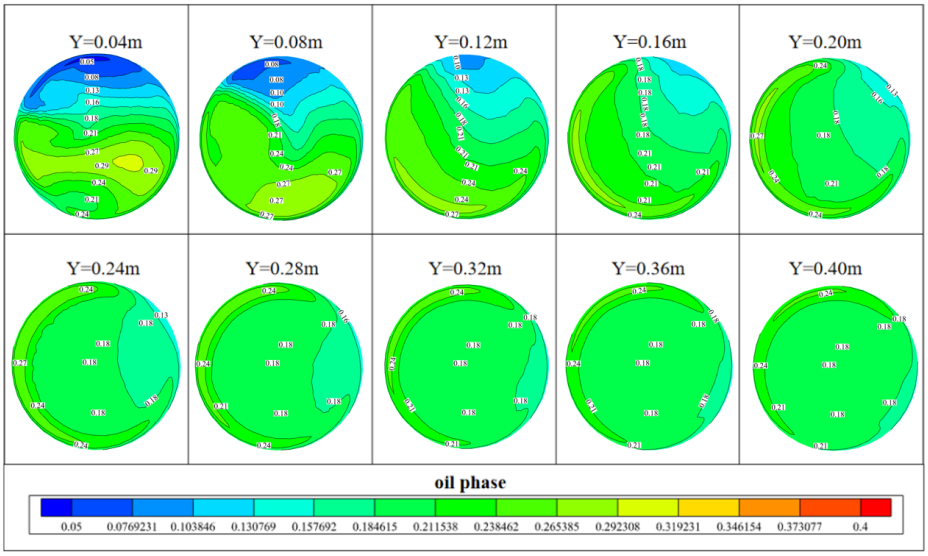


Figure 18. Phase distribution contour plots at cross sections of the outlet sections at different positions in the y-direction of the blind tee.

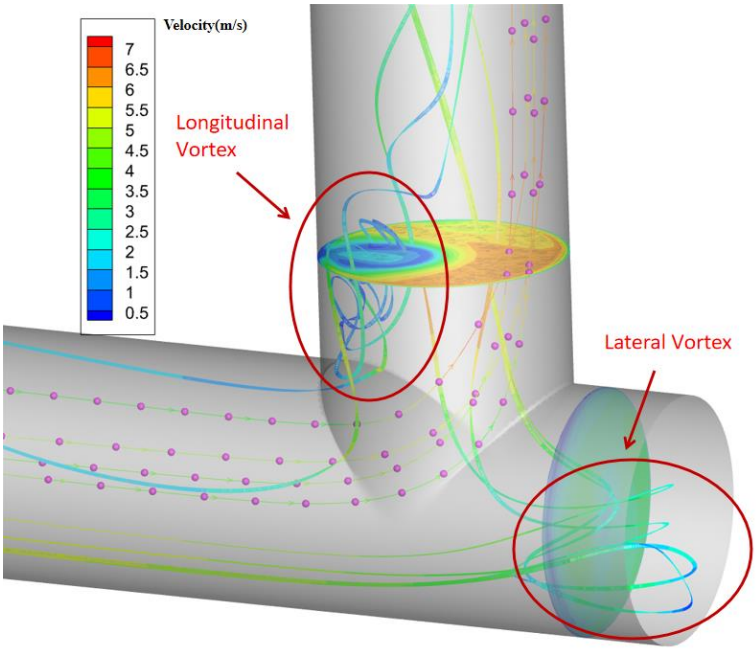


Figure 19. 3D streamline plot of the blind tee.

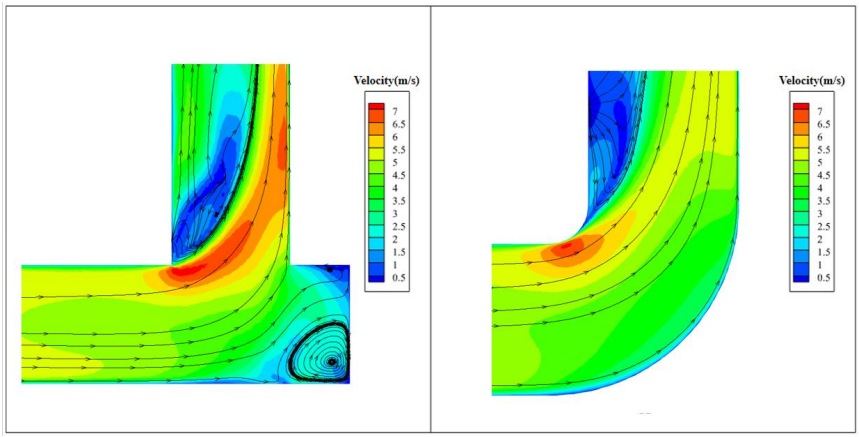


Figure 20. Comparative flow field plot of the blind tee and bent pipe.

To compare the differences in vortices between the two structures, vortex identification was performed on both structures. Existing vortex identification methods include the vorticity method, Q-criterion, λ_2 method, and Δ method. Among these, the Q-criterion is commonly used due to its lower computational cost and relatively consistent results. The Q-criterion is based on the analysis of the velocity gradient tensor. The formula for the Q-criterion is as follows:

$$Q = 0.5 \times \left(\|B\|_F^2 - \|A\|_F^2 \right) \tag{11}$$

In the formula, $\|B\|_F^2$ is the squared norm of matrix B, which is equal to the sum of the squares of all elements of matrix B. Matrices A and B are the symmetric and antisymmetric parts of the velocity gradient tensor, respectively, defined as follows:

$$A = 0.5 \times \left(\Delta V + \Delta V^T \right) \tag{12}$$

$$B = 0.5 \times \left(\Delta V - \Delta V^T \right) \tag{13}$$

$$\Delta V = \begin{pmatrix} U_X & U_Y & U_Z \\ V_X & V_Y & V_Z \\ W_X & W_Y & W_Z \end{pmatrix} \tag{14}$$

Figure 21 shows the vortex flow obtained using the Q-criterion for both the blind tee and the bent pipe. It is evident that the vortex in the vertical pipe section of the blind tee is wider and longer than that in the bent pipe, and a larger vortex region exists at the blind end. This explains why the rectification effect of the blind tee is significantly better than that of the bent pipe. To evaluate the applicability of blind tees in industrial settings, it is necessary to compare their pressure drop characteristics with those of elbows. By measuring the average pressure 50 mm upstream of the outlet, the pressure for the blind tee is found to be 596.311 Pa, while that for the elbow is 535.876 Pa. The comparison indicates that under identical inlet conditions, the pressures near the outlet are similar for both structures. This suggests that the pressure drop characteristics of blind tees are highly consistent with those of elbows, validating the feasibility of using blind tees in industrial applications to enhance the rectification performance of oil–water two-phase flow.

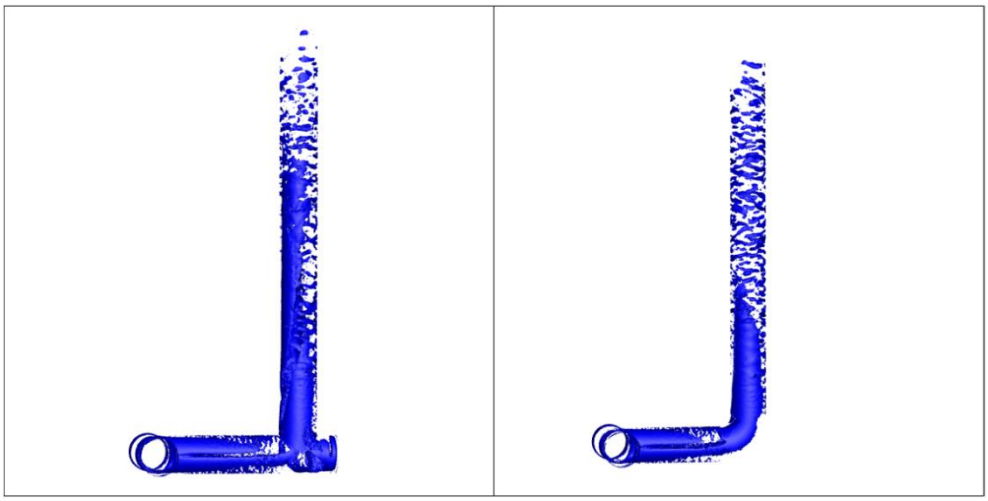


Figure 21. The internal vortex patterns of a blind tee (**left**) and an elbow pipe (**right**).

3.4.3. Comparison of Experimental and Numerical Simulation Conclusions

By comparing the experimental vector field and the numerical simulation vector field in the blind end region, it can be observed that the numerical simulation results exhibit

good agreement with the experimental data in terms of fluid backflow vector direction and rotational motion characteristics (Figure 22). This consistency indicates that the numerical simulation can accurately reproduce the flow characteristics within the blind end region. Furthermore, this agreement demonstrates that numerical simulations not only provide a reasonable prediction of the blind end flow field structure but also offer more detailed flow parameter information, serving as a reliable foundation for further optimization of the rectification performance of the blind tee.

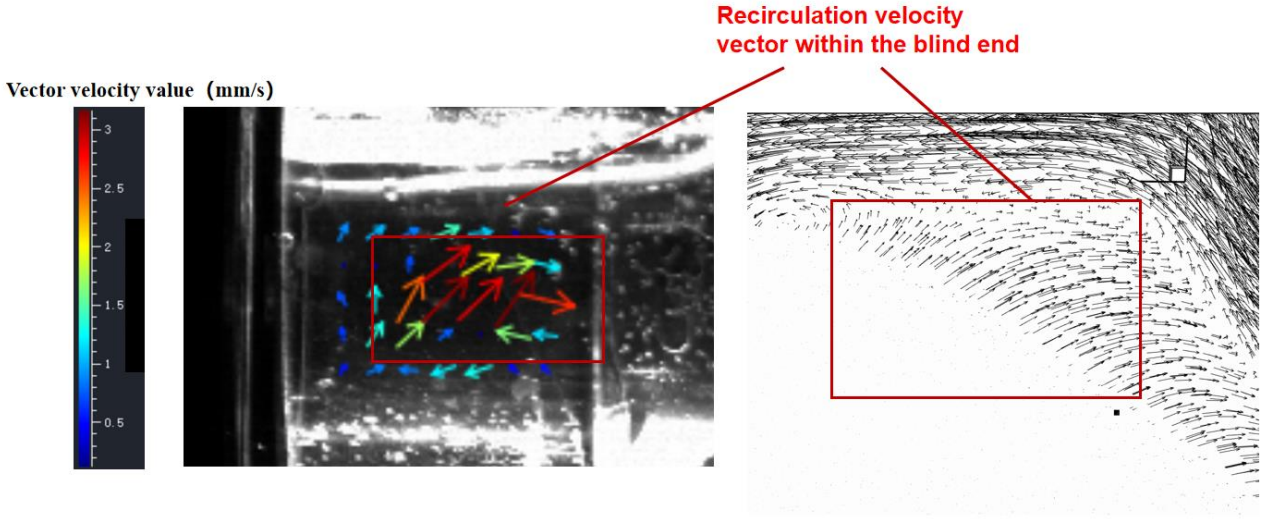


Figure 22. The experimental vector field and the numerical simulation vector field in the blind end region.

3.5. Effects of Different Conditions on the Oil–Water Rectification Efficiency of Blind Tees

3.5.1. Effect of Blind Tee Length

To investigate the effect of blind tee blind end length (BTL) on oil–water rectification performance, five blind tee models with blind end lengths of D, 1.5D, 2D, 2.5D, and 3D were established and analyzed through numerical simulations. As shown in Figure 23, with increasing blind end length, both the longitudinal vortex at the bend and the lateral vortex at the blind end expand; however, the velocity within the vortex region decreases. Figure 24 presents the phase distribution at y = 0.35 m in the vertical pipe for different blind end lengths, while Figure 25 provides statistical data on rectification coefficients. A comparison reveals that the rectification coefficient S increases with blind end length, indicating that rectification performance deteriorates as the blind end length increases. The optimal blind end length for rectification, corresponding to the lowest S value, was found to be 1.5D. Figure 26 illustrates the cross-sectional average velocity and turbulent dissipation rate at the midpoint of the blind end for each blind tee. By analyzing these parameters, the underlying mechanisms affecting rectification performance can be elucidated. As the blind end length increases, the velocity of the fluid entering the blind end decreases significantly, accompanied by a reduction in turbulent dissipation rate. This suggests that while vortex structures grow larger with increasing blind end length (Figure 23), their intensity weakens considerably, resulting in diminished oil–water mixing and reduced rectification efficiency, albeit with lower energy losses. Conversely, for very short blind ends, both velocity and turbulent dissipation rate within the blind end increase significantly, indicating strong vortex intensity. However, this leads to excessive energy dissipation, causing insufficient residual kinetic energy in the oil–water two-phase flow upon entering the vertical section. Consequently, the remaining energy is inadequate to counteract the combined effects of gravity and pipe wall friction, resulting in a large-phase distribution gradient across the cross section, which adversely affects rectification efficiency. Therefore,

in practical engineering applications, an optimal blind end length should be determined by balancing vortex structure size, energy dissipation, and rectification performance to achieve an efficient design.

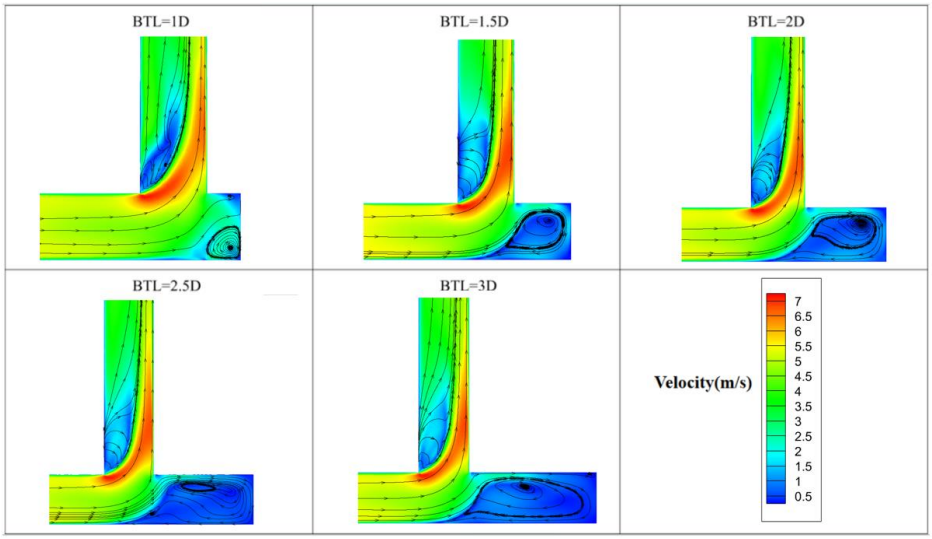


Figure 23. Streamline diagrams of blind tees with different blind end lengths.

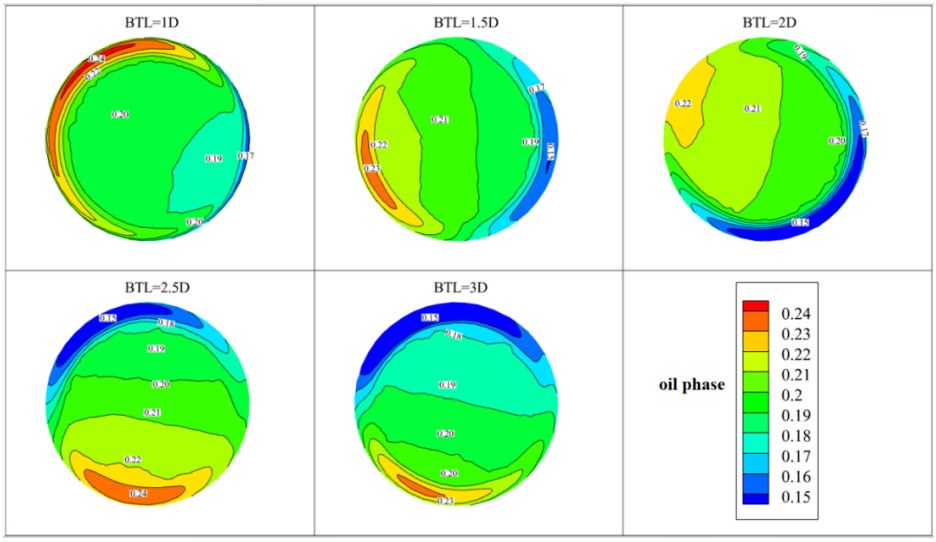


Figure 24. Phase distribution contour maps at y = 0.35 m for vertical pipes with different blind end lengths in blind tees.

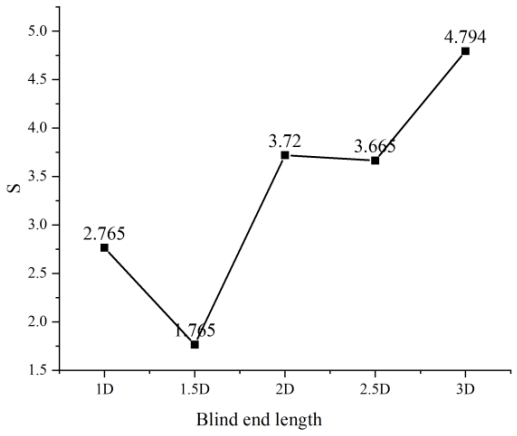


Figure 25. Rectification coefficients of blind tees with different blind end lengths.

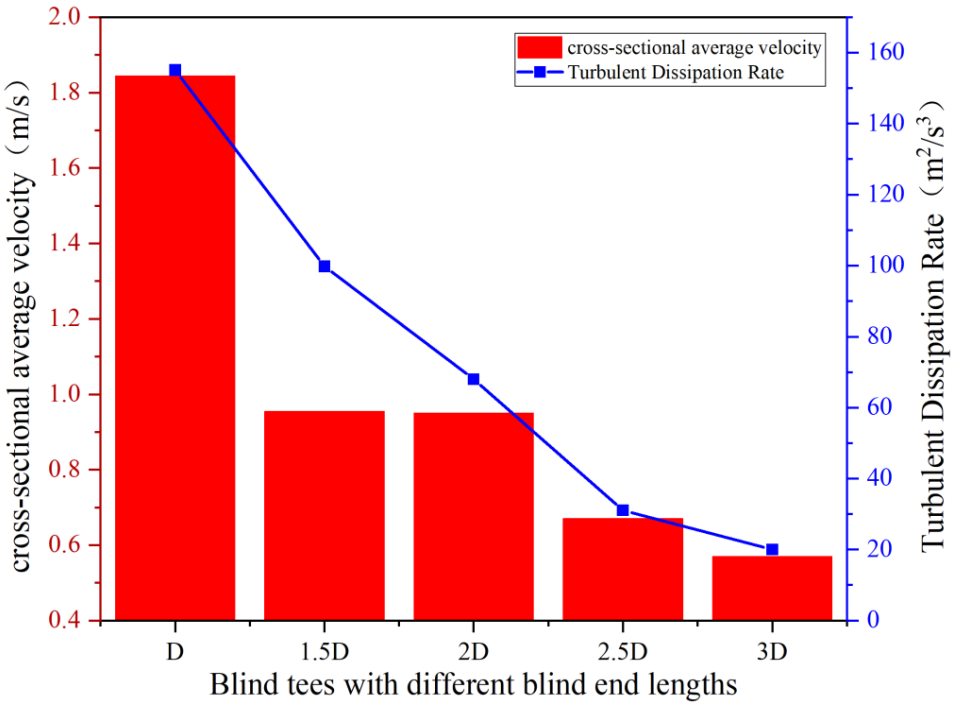


Figure 26. Cross-sectional average velocity and turbulent dissipation rate at the blind ends of different types of blind tees.

3.5.2. Effect of Flow Velocity

To investigate the effect of different inlet velocities on the oil–water rectification efficiency of a blind tee with a blind end length of D, oil–water mixtures with inlet velocities of 1 m/s, 2 m/s, 3 m/s, 4 m/s, and 5 m/s were introduced. As shown in Figure 27, when the velocity increases from 1 m/s to 3 m/s, the vortices at the blind end become larger, but further increases in velocity reduce the vortex size because the high-speed fluid entering from the horizontal section suppresses vortex development. From the rectification coefficient at different inlet velocities (Figure 28), it can be observed that the rectification coefficient decreases with increasing velocity from 1 m/s to 5 m/s, but peaks at 3 m/s, indicating the worst rectification efficiency at this velocity. Combining the analysis of Figure 27, Figure 28, Figure 29, it is evident that at 3 m/s, the vortex generated at the blind end has a width along the *X*-axis approximately equal to the length of the blind end. This results in the blind end being sealed off by the vortex, causing most of the fluid to bypass the blind end and enter the vertical pipe directly, thereby reducing the area affected by the vortex and leading to poor rectification efficiency. This velocity is defined as the blind end sealing velocity. As the velocity increases further, the high-speed fluid from the horizontal section suppresses vortex development, resulting in smaller vortices and an increase in the fluid entering the blind end. Higher velocities enhance the fluid's kinetic energy, reduce the size of the vortices, but increase the vortex intensity and secondary flow velocity, thereby improving the disturbance of non-uniform distribution areas and enhancing oil–water rectification efficiency.

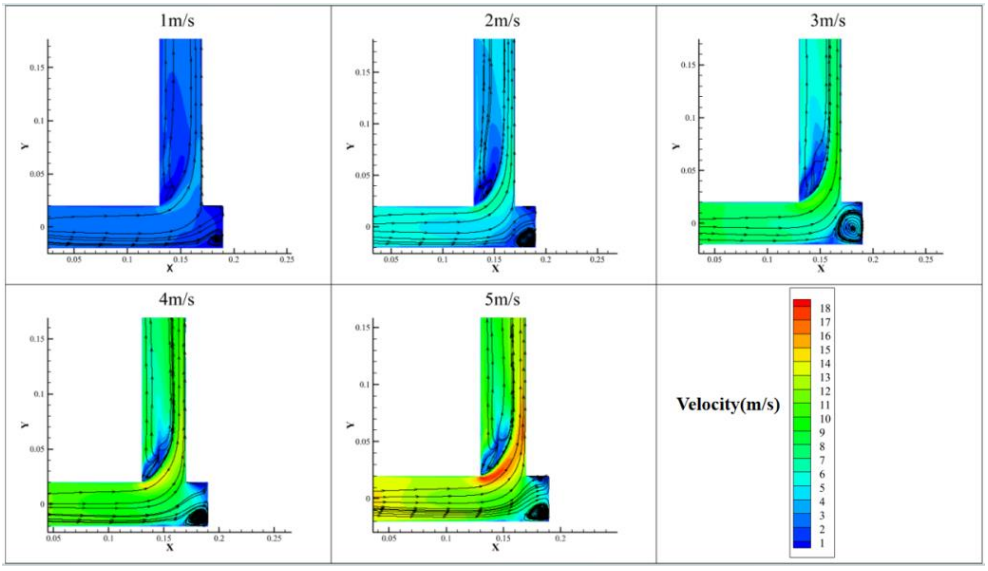


Figure 27. Streamline diagrams of blind tees at different inlet velocities.

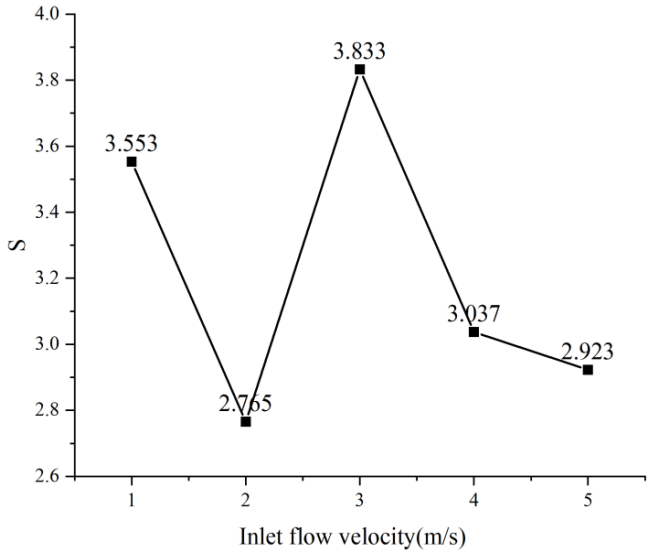


Figure 28. Rectification coefficients of blind tees at different inlet velocities.

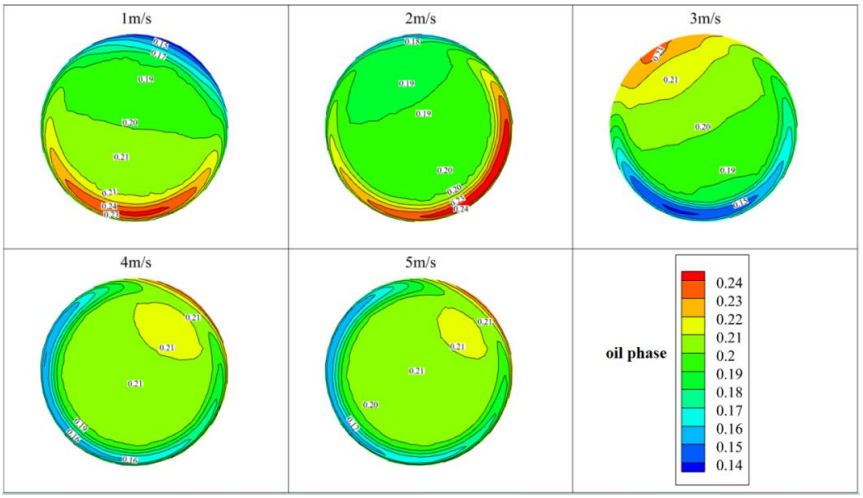


Figure 29. Phase distribution contour maps at y = 0.35 m in the vertical pipe for different inlet velocities.

3.5.3. Effect of Inner Diameter of the Vertical Pipe

There are still a large number of differential diameter blind tees in offshore oil transportation pipelines. This study investigated the effect of varying the internal diameter of the vertical pipe on oil–water rectification efficiency. Models of blind tees with vertical pipe diameters of 40 mm, 35 mm, 30 mm, 25 mm, and 20 mm were established for internal flow field analysis. As shown in Figure 30, as the vertical pipe diameter increases, the vortices at the blind end gradually become larger, and the flow velocity in the vertical section decreases. Figure 31 demonstrates that with increasing pipe diameter, the phase distribution at the cross section becomes more uneven. When the pipe diameter is 20 mm, the phase distribution achieves a very uniform state, indicating that higher fluid velocities in the vertical pipe lead to earlier uniform phase distribution. Figure 32 compares the rectification coefficients of blind tees with different vertical pipe diameters, revealing that smaller vertical pipe diameters result in lower rectification coefficients and better rectification efficiency. The reason is that a vertical pipe diameter smaller than that of the horizontal pipe acts as a throttle. According to the continuity equation of pipe flow, a smaller diameter results in higher velocity, which in turn increases the longitudinal vortex intensity at the bend, thereby enhancing the effect of promoting more uniform phase distribution.

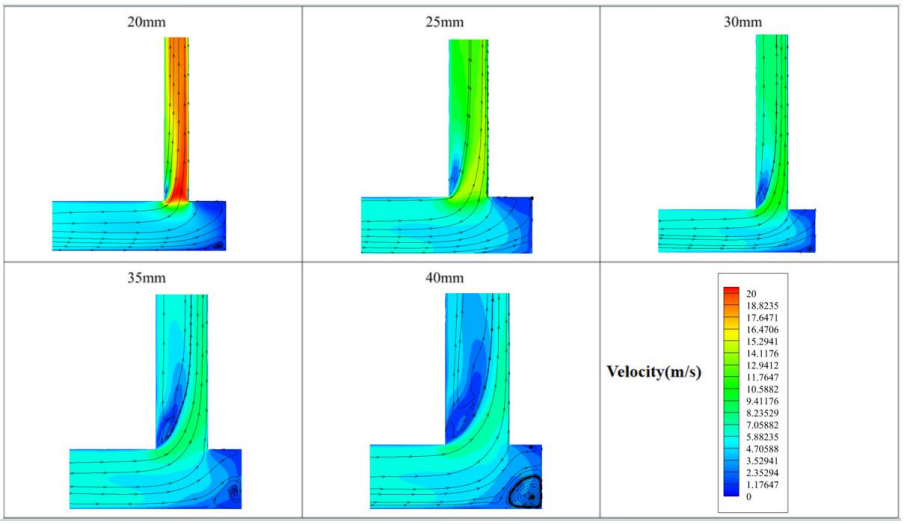


Figure 30. Streamline diagrams of blind tees with different vertical pipe diameters.

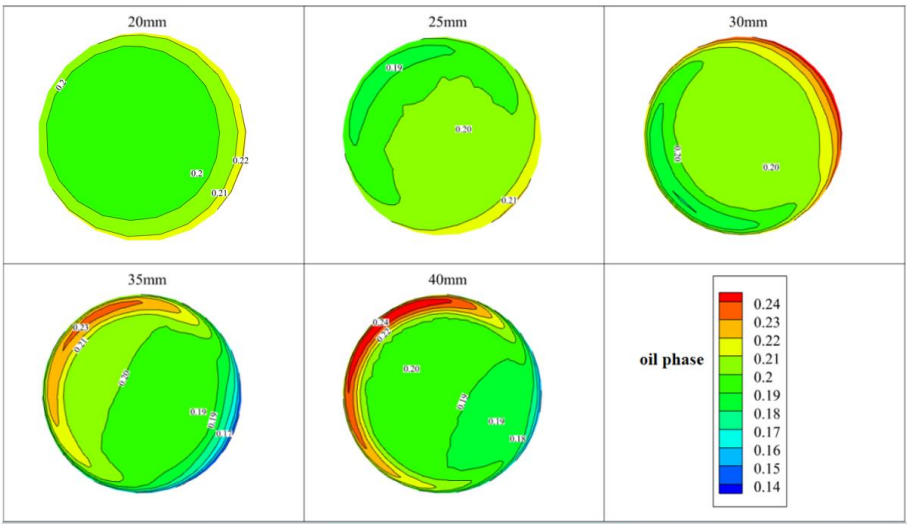


Figure 31. Phase distribution contour maps at y = 0.35 m in the vertical pipe for blind tees with different vertical pipe diameters.

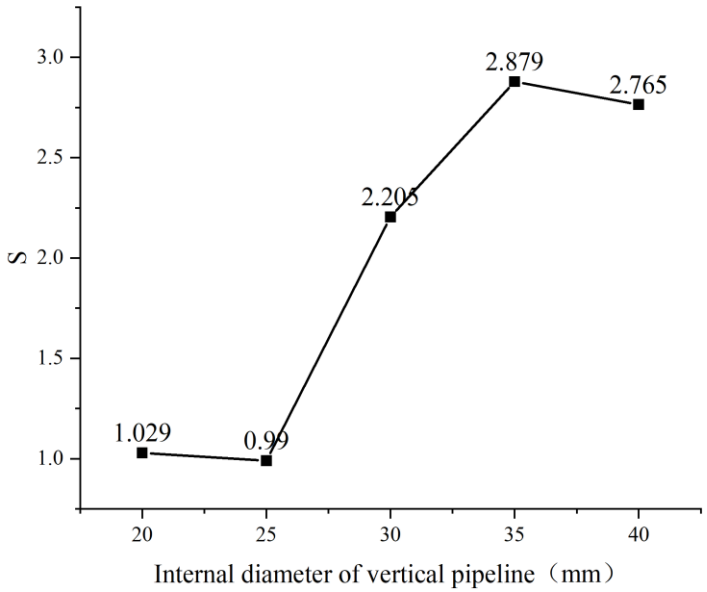


Figure 32. Rectification coefficients of blind tees with different vertical pipe diameters.

3.5.4. Effect of Oil Content

To investigate the effect of different oil contents on the rectification efficiency of blind tees, the oil content at the blind tee inlet was set to 5%, 10%, 15%, 20%, and 25%. As shown in Figure 33, the size of the vortices formed at the blind end is relatively consistent across different oil contents, but a larger low-velocity region is observed in the case of 25% oil content. Figure 34 clearly shows that higher oil content results in a more uneven phase distribution at the cross section. Figure 35 indicates that higher oil content leads to higher rectification coefficients, implying poorer rectification efficiency. As the oil content increases, the overall fluid density decreases, reducing the kinetic energy of the fluid at the same inlet velocity. This results in lower vortex intensity, which in turn reduces the disturbance to the oil–water two-phase flow, requiring a longer flow region for uniform phase distribution.

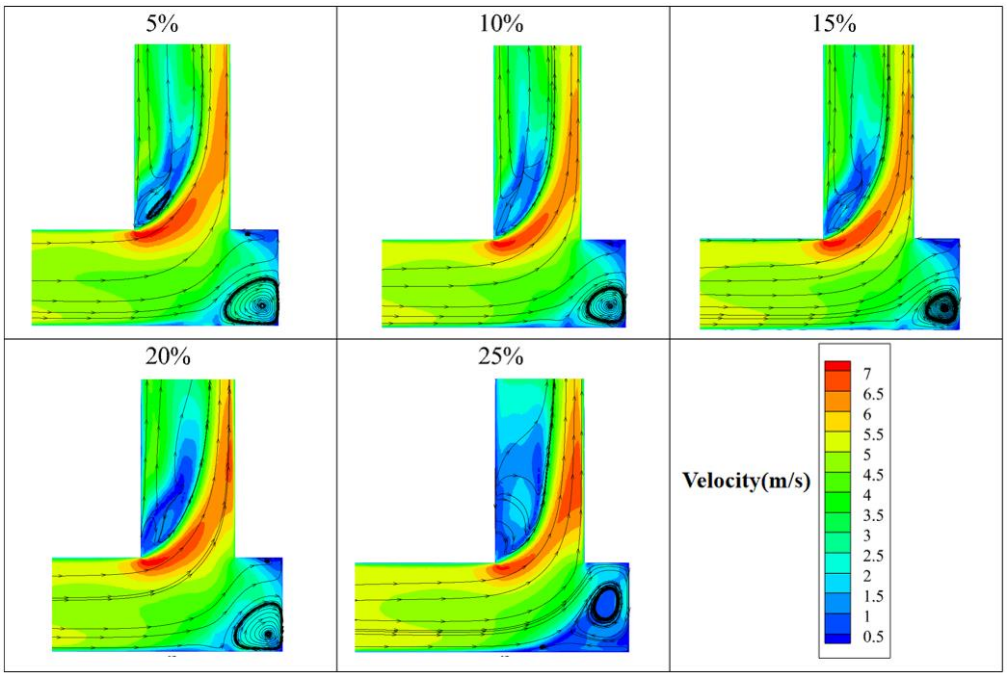


Figure 33. Streamline diagrams of blind tees at different oil content levels.

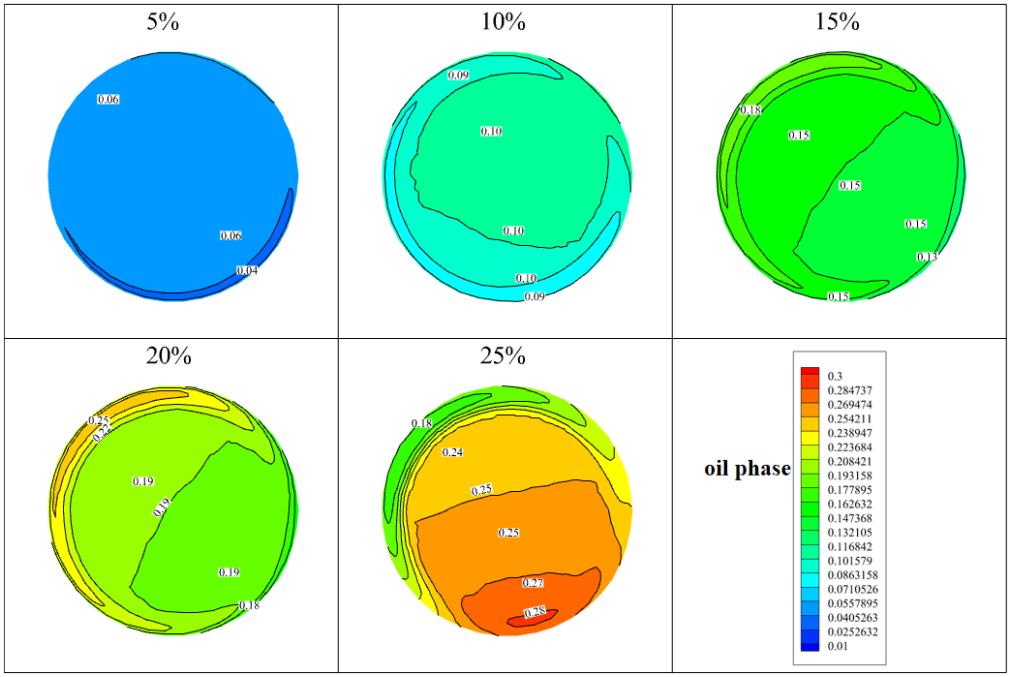


Figure 34. Phase distribution contour maps at y = 0.35 m in the vertical pipe for blind tees at different oil content levels.

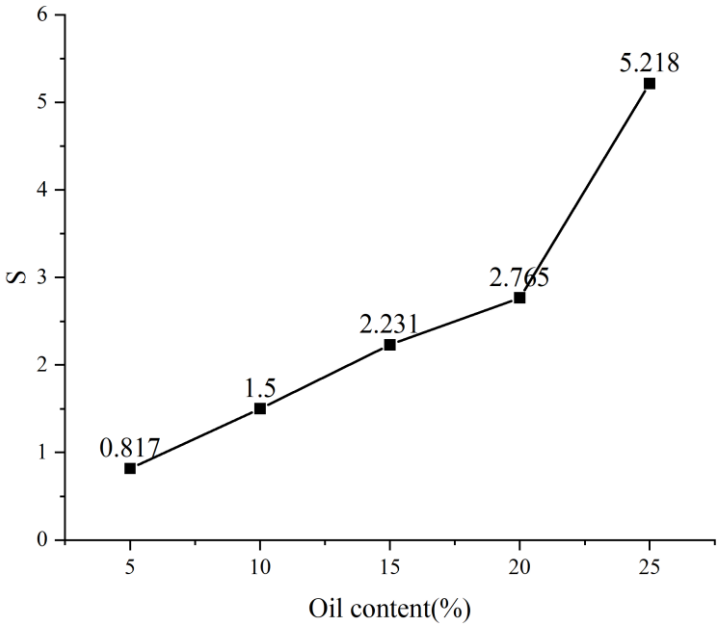


Figure 35. Rectification coefficients of blind tees at different oil content levels.

4. Conclusions

We defined the rectification coefficient S to assess the rectification performance of the device. Comparing the internal flow characteristics of blind tees and bends in oil–water systems, it was observed that bends generate only one large vortex inside, whereas blind tees generate two to three vortices. Due to the larger number and broader range of vortices inside blind tees, their rectification efficiency is significantly superior to bends. As the length of the blind end increases, the vortices within the blind tee grow larger. However, the elongation of the blind end results in increased wall frictional resistance and greater dissipation of kinetic energy during fluid flow, thereby deteriorating the rectification efficiency. At higher velocities, the fluid's kinetic energy increases. At the velocity typical

of blind-tee blind end closures, vortices formed at the blind end obstruct the entry of subsequent fluid, resulting in the poorest rectification efficiency. As velocity continues to increase, the vortices are suppressed, leading to smaller vortices but higher intensity, thereby improving the rectification efficiency of oil–water. Vertical pipes with an inner diameter smaller than horizontal pipeline diameters act as throttling devices. Smaller diameters result in higher velocities, increasing vortex intensity at bends and promoting more uniform phase distribution. Higher oil content correlates with poorer rectification efficiency. Through the research presented in this paper, it was found that replacing the bend with a specific blind tee in the oil–water two-phase flow measurement device under the same operating conditions increases the rectification efficiency by 76.68%, thereby significantly enhancing measurement accuracy.

5. Limitations of the Study and Future Research Directions

This study focused only on specific blind tee structures and operating conditions, without covering a broader range of structural forms and flow conditions, which may limit the applicability of the research conclusions. Additionally, due to limitations in the experimental setup, the experimental validation primarily provides qualitative results, lacking high-precision quantitative data support, which may affect the verification of the simulation results.

Future research can be further expanded in the following aspects: 1. Explore the impact of different geometric configurations (e.g., variable cross section blind ends, rounded blind ends) on flow characteristics, and analyze their rectification performance and mixing efficiency under various flow regimes of oil–water two-phase flow; 2. Design adaptive blind tee structures capable of automatically adjusting the opening, closing, or length of the blind end based on real-time flow conditions to meet rectification requirements under different operating scenarios; 3. Investigate the adaptability of blind tee structures under extreme conditions such as high pressure and high temperature.

Author Contributions: Conceptualization, C.C.; methodology, C.C.; formal analysis, C.C.; investigation, C.C. and Y.Z.; resources, Q.G.; data curation, Y.S. and Q.G.; writing—original draft preparation, C.C. and Y.C.; writing—review and editing, C.C. and Q.G. All authors have read and agreed to the published version of the manuscript.

Funding: This research received no external funding.

Data Availability Statement: Data were obtained from the China National Petroleum Corporation (CNPC) and are available from the authors with the permission of the CNPC.

Conflicts of Interest: Chen Cheng was employed by the Sinopec Natural Gas Branch. Qingming Gan and Yubin Su were employed by the Changqing Oilfield Branch Company. Yang Cheng was employed by the Jianghan Oilfield Branch Company. The authors declare that the research was conducted in the absence of any commercial or financial relationships that could be construed as potential conflicts of interest.

Nomenclature

ρ	fluid density, kg/m^3
K	turbulence kinetic energy, J/kg
t	time, s
$\overline{u_j}$	the mean velocity component in the -th direction, m/s
x_j	the spatial coordinate in the j-direction, m
μ	dynamic viscosity, Pa·s
μ_t	turbulent viscosity, Pa·s
Pr_K	the Prandtl number for turbulence kinetic energy

P_K	the generation rate of turbulence kinetic energy, W/m^3
G_b	the turbulence kinetic energy generated by buoyancy, m^2/s^3
ε	the dissipation rate of turbulence kinetic energy, m^2/s^3
Y_M	the influence of fluctuating dilation on turbulence dissipation rate, m^2/s^3
S	rectification coefficient
N	the number of sampling points
$\rho_{x_i y_j}$	the density of sampling points at different locations, kg/m^3
$\overline{\rho}$	the average density of the fluid entering the device, kg/m^3
α_q	the volume fraction of phase q
ρ_q	the density of phase q, kg/m^3
v_q	the velocity of phase q, m/s
τ_q	the stress tensor of the phase q, N/m^2

References

1. Yang, Y.; Ha, W.; Zhang, C.; Liu, M.; Zhang, X.; Wang, D. Measurement of high-water-content oil-water two-phase flow by electromagnetic flowmeter and differential pressure based on phase-isolation. *Flow Meas. Instrum.* **2022**, *84*, 102142. [CrossRef]
2. Zhang, J.; Xu, J.Y.; Wu, Y.X.; Li, D.H.; Li, H. Experimental validation of the calculation of phase holdup for an oil–water two-phase vertical flow based on the measurement of pressure drops. *Flow Meas. Instrum.* **2013**, *31*, 96–101. [CrossRef]
3. Brister, C.M. Wet gas performance of a low energy gamma ray multiphase meter. In Proceedings of the Offshore Technology Conference Brasil, Rio de Janeiro, Brazil, 29–31 October 2013; p. OTC-24352-MS.
4. Zheng, G.B.; Jin, N.D.; Jia, X.H.; Lv, P.J.; Liu, X.B. Gas–liquid two phase flow measurement method based on combination instrument of turbine flowmeter and conductance sensor. *Int. J. Multiph. Flow* **2008**, *34*, 1031–1047. [CrossRef]
5. Patankar, S.V.; Pratap, V.S.; Spalding, D.B. Prediction of turbulent flow in curved pipes. In *Numerical Prediction of Flow, Heat Transfer, Turbulence and Combustion*; Pergamon: Oxford, UK, 1983; pp. 147–159.
6. Ito, H. Flow in curved pipes. *JSME Int. J.* **1987**, *30*, 543–552. [CrossRef]
7. Di Liberto, M.; Di Piazza, I.; Ciofalo, M. Turbulence structure and budgets in curved pipes. *Comput. Fluids* **2013**, *88*, 452–472. [CrossRef]
8. Dutta, P.; Nandi, N. Effect of Reynolds number and curvature ratio on single phase turbulent flow in pipe bends. *Mech. Mech. Eng.* **2015**, *19*, 5–16.
9. Noorani, A.; Sardina, G.; Brandt, L.; Schlatter, P. Particle transport in turbulent curved pipe flow. *J. Fluid Mech.* **2016**, *793*, 248–279. [CrossRef]
10. Ayala, M.; Cimbala, J.M. Numerical approach for prediction of turbulent flow resistance coefficient of 90 pipe bends. *Proc. Inst. Mech. Eng. Part E J. Process Mech. Eng.* **2021**, *235*, 351–360. [CrossRef]
11. Jarrahi, M.; Castelain, C.; Peerhossaini, H. Secondary flow patterns and mixing in laminar pulsating flow through a curved pipe. *Exp. Fluids* **2011**, *50*, 1539–1558. [CrossRef]
12. Kim, J.; Yadav, M.; Kim, S. Characteristics of secondary flow induced by 90-degree elbow in turbulent pipe flow. *Eng. Appl. Comput. Fluid Mech.* **2014**, *8*, 229–239. [CrossRef]
13. Pouraria, H.; Seo, J.K.; Paik, J.K. Numerical study of erosion in critical components of subsea pipeline: Tees vs. bends. *Ships Offshore Struct.* **2017**, *12*, 233–243. [CrossRef]
14. Chen, X.; McLaury, B.S.; Shirazi, S.A. Numerical and experimental investigation of the relative erosion severity between plugged tees and elbows in dilute gas/solid two-phase flow. *Wear* **2006**, *261*, 715–729. [CrossRef]
15. Han, F.; Ong, M.C.; Xing, Y.; Li, W. Three-dimensional numerical investigation of laminar flow in blind-tee pipes. *Ocean. Eng.* **2020**, *217*, 107962. [CrossRef]
16. Ma, Y.; Li, C.; Pan, Y.; Hao, Y.; Huang, S.; Cui, Y.; Han, W. A flow rate measurement method for horizontal oil-gas-water three-phase flows based on Venturi meter, blind tee, and gamma-ray attenuation. *Flow Meas. Instrum.* **2021**, *80*, 101965. [CrossRef]
17. Rammohan, A.; Bhakta, A.; Natrajan, V.; Ward, J.; Kumar, M. Flow swirl and flow profile measurement in multiphase flow. In Proceedings of the 31st International North Sea Flow, Tonsberg, Norway, 22–25 October 2013.
18. Millington, D. Evaluation of blind-t mixing effectiveness within two-phase gas-viscous oil flow using electrical capacitance tomography. In Proceedings 10th North American Conference on Multiphase Technology, Banff, AB, Canada, 8–10 June 2016; p. BHR-2016-399.
19. Hjertaker, B.T.; Tjugum, S.A.; Hallanger, A.; Maad, R. Characterization of multiphase flow blind-T mixing using high speed gamma-ray tomometry. *Flow Meas. Instrum.* **2018**, *62*, 205–212. [CrossRef]
20. Valdés, J.P.; Kahouadji, L.; Matar, O.K. Current advances in liquid–liquid mixing in static mixers: A review. *Chem. Eng. Res. Des.* **2022**, *177*, 694–731. [CrossRef]

21. Yan, S.; Lv, F.; Wang, B.; Dong, X.; Yang, X.; Ma, L.; Chen, S.; Han, B.; Bai, Z. Mixing characteristics and intensification mechanism of an improved swirl jet mixer for high phase ratios. *J. Ind. Eng. Chem.* **2024**, *135*, 457–470. [CrossRef]
22. Meng, H.; Meng, T.; Yu, Y.; Wang, Z.; Wu, J. Experimental and numerical investigation of turbulent flow and heat transfer characteristics in the Komax static mixer. *Int. J. Heat Mass Transf.* **2022**, *194*, 123006. [CrossRef]
23. Chakleh, R.; Azizi, F. Performance comparison between novel and commercial static mixers under turbulent conditions. *Chem. Eng. Process. -Process Intensif.* **2023**, *193*, 109559. [CrossRef]

Disclaimer/Publisher's Note: The statements, opinions and data contained in all publications are solely those of the individual author(s) and contributor(s) and not of MDPI and/or the editor(s). MDPI and/or the editor(s) disclaim responsibility for any injury to people or property resulting from any ideas, methods, instructions or products referred to in the content.